Rapid Communications

Evidence of the direct-to-indirect band gap transition in strained two-dimensional WS_2, MoS_2, and WSe_2

E. Blundo,[1] M. Felici,[1] T. Yildirim,[2] G. Pettinari,[3] D. Tedeschi,[1] A. Miriametro,[1] B. Liu,[2] W. Ma,[2] Y. Lu,[2,4] and A. Polimeni[1,*]

[1]*Dipartimento di Fisica, Sapienza Università di Roma, 00185 Roma, Italy*

[2]*Research School of Electrical, Energy and Materials Engineering, College of Engineering and Computer Science, The Australian National University, Canberra, ACT 2601, Australia*

[3]*Institute for Photonics and Nanotechnologies, National Research Council, 00156 Roma, Italy*

[4]*ARC Centre of Excellence in Future Low-Energy Electronics Technologies (FLEET) ANU node, Canberra, ACT 2601, Australia*

(Received 15 September 2019; revised manuscript received 18 November 2019; published 23 January 2020)

We report a strain-induced direct-to-indirect band gap transition in mechanically deformed WS_2 monolayers (MLs). The necessary amount of strain is attained by proton irradiation of bulk WS_2 and the ensuing formation of 1-ML-thick, H_2-filled domes. The electronic properties of the curved MLs are mapped by spatially and time-resolved microphotoluminescence, revealing the mechanical stress conditions that trigger the variation of the band gap character. This general phenomenon, also observed in MoS_2 and WSe_2, further increases our understanding of the electronic structure of transition metal dichalcogenide MLs and holds a great relevance for their optoelectronic applications.

DOI: 10.1103/PhysRevResearch.2.012024

The properties of solids are very sensitive to variations in bond length ensuing a mechanical deformation or stress. This is especially true in the case of two-dimensional (2D) crystals [such as graphene, hexagonal-BN, and transition metal dichalcogenide (TMD) monolayers (MLs)] due to their all-surface nature [1]. Particularly appealing in TMD MLs is the strong coupling between the valley/spin/orbital degrees of freedom and the lattice structure, reflected in the strong response of their electronic [2], transport [3], and optical [4] properties to strain. In particular, nonuniform strains turn out to be extremely relevant: On the one hand, strain gradients in 2D TMDs can lead to a coherent drift of photogenerated carriers, relevant for photon harvesting [5,6]. On the other hand, a nonuniform strain gives rise to pseudoelectromagnetic fields enabling the observation of novel transport phenomena [7].

In this Rapid Communication, we report a study of the band gap character in mechanically deformed WS_2, MoS_2, and WSe_2 2D crystals. The deformation follows the local blistering over a micron-sized region of the upper layer of bulk flakes exposed to proton irradiation [8]. The resulting spherically shaped MLs, hereafter named domes, host nonuniform and high strain fields, evaluated by finite-element method (FEM) calculations and consistently compared with micro-Raman measurements. Steady-state and time-resolved microphotoluminescence (micro-PL) mapping of the band gap states over the surface of a single dome unveils dramatic changes in the emission energy, intensity, and decay time. Such changes are related to the built-in tensile strain of the dome and are ascribed to a strain-induced direct (K_{CB}-K_{VB})-to-indirect (K_{CB}-Γ_{VB}) band gap transition (CB and VB stand for conduction and valence band, respectively). The strain conditions that determine the crossover of the VB Γ and K states are found.

The dome-shaped membranes under study were created from bulk MX_2 flakes (where M = W or Mo, and X = S, Se, or Te), which were mechanically exfoliated on Si substrates and then proton irradiated with a low-energy beam [8,9]. Here, we focus on WS_2. The accelerated protons penetrate through the flake surface and H_2 forms just one layer beneath the surface, as described in Ref. [8]. As a consequence of the balance between the gas expansion, the van der Waals forces holding the S-W-S planes together and the material's elastic properties, localized swelling of just 1 ML takes place, resulting in the formation of atomically thin and spherically shaped domes [see the atomic force microscope (AFM) image in Fig. 1(a)]. The domes cage highly pressurized H_2 and are durable owing to the impermeability to H_2 of TMD MLs [10]. As shown in Fig. 1(a), domes with different size stud the flake's surface, nevertheless featuring an aspect ratio, $h_m/R = 0.16 \pm 0.02$, independent of R [8,11] (R is the footprint radius and h_m is the maximum height of the domes). The domes were characterized by micro-Raman and micro-PL experiments at room temperature using a 532-nm laser as the excitation source. A diffraction grating monochromator coupled to a Si-CCD was used for spectral analysis of the signal. Time-resolved micro-PL at 50 K was performed using a supercontinuum laser tuned at 532 nm with ~50 ps pulse width and 77.8 MHz repetition rate. The signal was time analyzed by a Si avalanche photodiode (APD) with 250 ps temporal resolution. Spatially resolved optical measurements were performed in backscattering configuration via a 100×

*Corresponding author: antonio.polimeni@roma1.infn.it

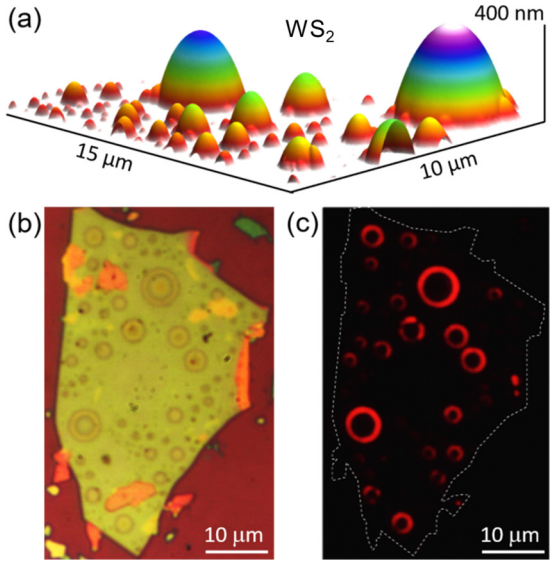

FIG. 1. (a) 3D AFM image of a bulk WS_2 flake irradiated with protons (dose $d_H = 4 \times 10^{16}$ protons/cm^2), showing the formation of almost perfectly spherical domes. (b) Optical image of a WS_2 flake, where many relatively large domes formed after proton irradiation ($d_H = 5 \times 10^{16}$ protons/cm^2). (c) Laser-excited red luminescence coming from the same flake shown in (b).

objective with numerical aperture (NA) = 0.9, resulting in a laser spot with a standard deviation equal to $0.23 \pm 0.01\ \mu$m [12]. Finally, the strain tensor over the dome's surface was computed via FEM calculations [8].

Figure 1(b) shows the optical microscope image of a proton-irradiated WS_2 flake acquired with a 50 × (NA = 0.5) objective. The outer circular borders locate the domes' footprint while the internal patterns of each dome are due to interference effects between the light reflected by the dome top surface and the flat WS_2 flake underneath [8]. Figure 1(c) shows an optical image of the same flake, excited by a defocused 532-nm laser. The image was acquired at room temperature by filtering out the laser, thus letting the red luminescence (at ∼690 nm) generated by the domes be revealed. Peculiarly, the brightly emitting region is restricted to an outer ringlike area independently of the dome footprint. This excludes interference (which would be largely dependent on the dome size) to be the main origin of the observed luminescence pattern, differently from what recently reported in WS_2 bubbles obtained after annealing of chemical-vapor-deposition-grown MLs [13]. In that work, interference effects are likely enhanced by the SiO_2 substrate located right beneath the ML bubbles and strongly modulate the emission. On the contrary, in the present case, the peculiar ringlike emitting area stems from the strain field acting over the domes, as detailed in the following.

To model the spatial evolution of the strain tensor and the height profile of the domes we performed FEM calculations within the framework of the nonlinear membrane theory [8,14,15]. The AFM-derived radius and height of the domes and the elastic properties of the material were used as input parameters. Figure 2(a) (left axis) successfully compares the experimental (circles) and calculated (solid line) height profile along a radius ($0 \leqslant r \leqslant R$, where r is the position with

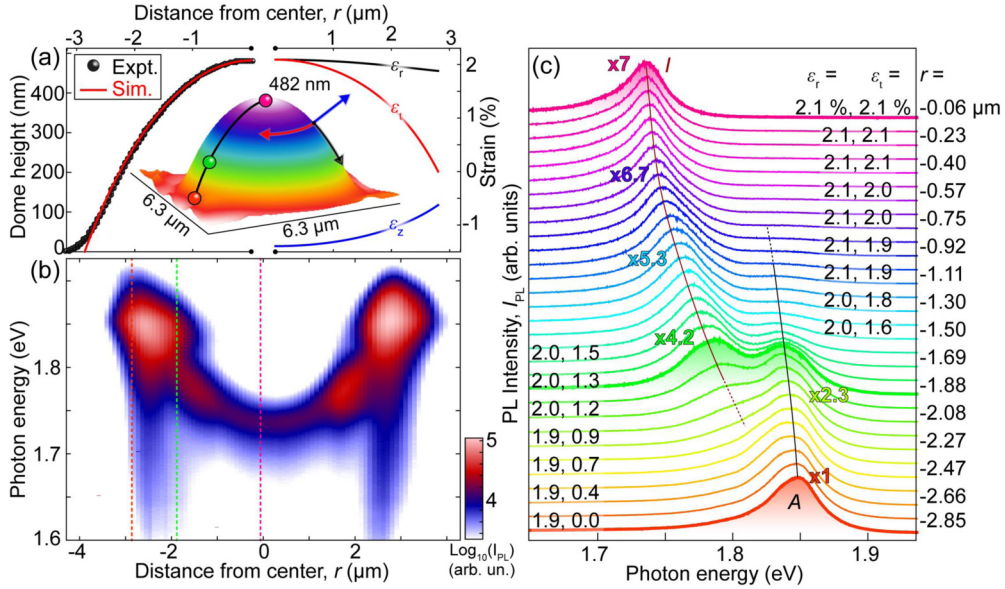

FIG. 2. (a) Left: Height profile of a WS_2 dome formed after irradiation with 4×10^{16} protons/cm^2, measured by AFM (black dots; the AFM image is shown as inset), and computed by FEM calculations (solid red line). Right: Dependence along the dome radius of the strain tensor components, represented as color-coded arrows in the inset. The three dots (purple: top; green: intermediate; orange: edge) correspond to the positions displayed as dashed lines in (b) and to the shadowed spectra in (c). (b) Micro-PL scan (with steps of 80 nm) along a diameter of the dome displayed in (a), performed at 297 K. The horizontal axis indicates the laser spot position with respect to the dome center, and the vertical axis indicates the emitted photon energy. The base-10 logarithm of the micro-PL intensity is shown in a false color scale. (c) Normalized emission spectra of the dome as the laser spot is scanned from the dome's left edge (bottom) to its apex (top). Intensity factors are displayed for some selected spectra. Spectra are labeled with the laser spot position and with the values of the radial (ε_r) and circumferential (ε_t) strain components. The solid lines follow the energy shift of the direct (A, black line) and indirect (I, red line) exciton transition.

respect to the center) of the WS_2 dome, whose AFM image is shown in the inset. The right axis of Fig. 2(a) displays the calculated r dependence of the principal components of the strain tensor—namely, along the circumferential (ε_t) and radial (ε_r) in-plane directions [14] and along the perpendicular (ε_z) out-of-plane direction. At the dome's summit, the (tensile) strain is isotropic biaxial ($\varepsilon_t = \varepsilon_r = 2.09\%$), in agreement with Hencky's model [4,8,14,16], whereas at the dome edges—where $\varepsilon_t = 0$—strain is uniaxial. The negative value of ε_z all over the surface is caused by the membrane thinning following the in-plane tensile strain. The strain field across the dome is expected to induce remarkable changes in the electronic properties of the curved TMD membrane [5,17–27], giving rise to the peculiar phenomenology displayed in Fig. 1(c). Spatially resolved micro-PL/Raman measurements were then performed on the dome shown in Fig. 2(a), which was chosen since its size ($R = 2.85\,\mu$m) is much larger than the probing laser spot (0.23 μm) [12], thus minimizing diffraction effects. However, it is important to note that the dome aspect ratio and, consequently, the strain distribution remain unchanged with the dome size [8], ensuring the general significance of the following results.

To begin with, the micro-Raman measurements described in the Supplemental Material [28] show a progressive softening of the in-plane and out-of-plane vibrational modes while moving from the edge towards the center of the dome, in agreement with the expected tensile-strain increase [13,29,30]. However, the full extent of the effects of strain on the optoelectronic properties of TMD MLs can only be appreciated by looking at the dome's PL emission. Figure 2(b) depicts a room-temperature micro-PL scan taken along a diameter of the dome displayed in the inset of Fig. 2(a). The vertical axis indicates the energy of the emitted photons, while the base-10 logarithm of the PL intensity is shown in a false color scale. On moving from the edge toward the summit of the dome, the marked redshift of the emission wavelength is accompanied by an equally striking decrease (about a factor 10) of the PL intensity. Figure 2(c) describes in more detail the dramatic changes of the emission spectra from the dome's edge ($r = -2.85\,\mu$m) to the dome's center ($r = -0.06\,\mu$m). Each spectrum is labeled also with the pertinent values of the radial and circumferential strain components [see Fig. 2(a)]. The micro-PL spectra recorded close to the edge are dominated by the direct (K_{CB}-K_{VB}) band gap exciton (A), whose energy (equal to 2.00 eV in a strain-free reference WS_2 ML [8]) is redshifted by the tensile strain exerted on the dome. As the excitation laser moves toward the center, the direct exciton keeps redshifting and concomitantly a new, less intense band, labeled I, takes over and eventually dominates the spectrum. We ascribe this band to the K_{CB}-Γ_{VB} *indirect* band gap exciton. In fact, as predicted by numerous theoretical works [5,17,18,20–24], the presence of strain in TMD MLs [17,18,20–25,27] and bilayers [31,32] should result in a significant reordering of the energies of the critical points of the band structure. In particular, for tensile biaxial strains $\varepsilon > 1\%$ in WS_2 MLs [17,18,20–22,24,25,27], the valence band maximum should change from the K to the Γ point of the reciprocal space. Even though this change (i) is expected to occur for values of ε that are well within reach of current strain modulation techniques [31,33–35], and (ii) should result in

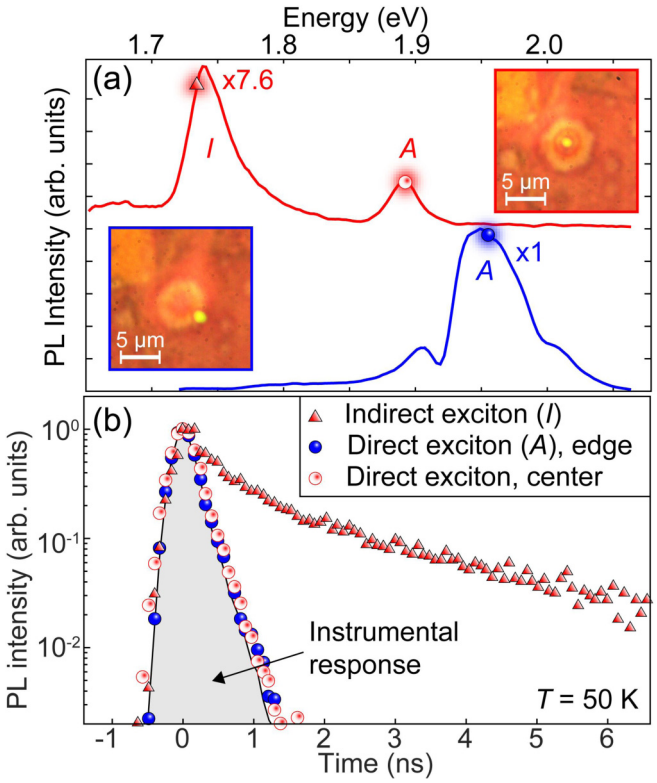

FIG. 3. (a) $T = 50$ K micro-PL spectra recorded at the center (red) and edge (blue) of a WS_2 dome. The insets are optical microscope images of the dome, showing the laser spot position corresponding to each spectrum. The symbols superimposed on the spectra indicate the energy at which the signal temporal decay shown in (b) was recorded. (b) Temporal evolution of the micro-PL signal relative to the specific photon energy and position on the dome highlighted in (a). The gray-shaded area refers to the exciting laser decay curve and sets the temporal resolution.

rather dramatic variations of the optical properties of the material, the currently available experimental evidence of this direct-to-indirect transition is either not particularly apparent [36–39] or absent [13,34,35,31]. This is possibly due to a less-than-perfect adhesion between the sample and the strain-inducing devices employed in some of the previous studies, resulting in an incomplete transfer of the applied stress to the TMD ML. In the present work, however, this is not an issue, as large biaxial strains—in the range between 1% and 3%—are induced by the pressure exerted on the TMD ML by the H_2 gas trapped and perfectly sealed within the dome.

To confirm the previous attributions, we investigated the temporal decay of the micro-PL signal of WS_2 domes. These were cooled down at 50 K to minimize the contribution of nonradiative decay channels [40]. Interestingly, the reduction of the dome's volume at cryogenic temperatures [8]—due to the contraction of the H_2 gas trapped inside the dome—is nearly brought to a halt by the deposition of a thin methylpentane layer on the sample surface (see Supplemental Material [28]), thus making it possible to spatially resolve the PL signal from different zones of the dome. Figure 3(a) shows the micro-PL spectra of a WS_2 dome recorded at the edge (where the A exciton dominates) and center (where the I

exciton can be observed along with the redshifted A exciton recombination); see pictures in the insets. Figure 3(b) shows the micro-PL decay curve relative to the different transitions displayed in Fig. 3(a). Most notably, the A and I excitons exhibit largely different temporal behaviors: The decay time of the A exciton is instrument limited ($<$250 ps), consistent with other reports [40,41]. Instead, the I exciton shows a much longer temporal decay that can be fitted by a double exponential function with two decay times equal to (0.40 ± 0.06) ns and (2.9 ± 0.7) ns, which clearly points to an indirect optical transition [41].

We now establish the strain conditions that induce the K-Γ crossover in the VB. This is an especially important aspect with regard to the optoelectronic properties of TMD MLs and to the enormous potential that mechanical stress holds to engineer those properties. For instance, application of a seamless gradient of strain in these materials could be exploited as an efficient broadband concentrator of photogenerated carriers in flexible solar cells [5]. Nevertheless, the occurrence of a strain-induced transition in the band gap character may affect both the absorption/emission properties and the carrier dynamics characteristics of devices based on TMD MLs. Furthermore, in the present case, the strain gradient enables the spatial concentration of long-lived k-indirect excitons with potential benefit for creating excitonic Bose condensates [42].

Figure 4(a) illustrates a micro-PL experiment performed on a single dome, highlighting the relevant physical processes discussed next. Figure 4(b) shows the peak energy $E_{A,I}$ of the A and I excitonic transitions derived from the same dome of Fig. 2 as a function of the "in-plane" strain $\varepsilon_p = \varepsilon_r + \varepsilon_t$. This choice is grounded on the hypothesis that each of the two planar strain components brings a similar effect on the ML band gap [17]. Moreover, for biaxially strained TMDs, $\varepsilon_z = -\frac{D_{13}}{D_{33}}\varepsilon_p$, where D_{13} and D_{33} are the pertinent components of the elasticity matrix [8,43]. Thus, as discussed in the Supplemental Material [28] the strain dependence of the energies of the A and I excitons can be written as

$$E_{A,I}(\varepsilon_p) = E_{A,I}(0) - \Delta_{A,I}\varepsilon_p, \tag{1}$$

where $\Delta_{A,I}$ is the shift rate with strain of the A (I) exciton. To correctly interpret the data shown in Fig. 4(b), however, we also have to consider that the continuous variation of the strain field on the dome surface [Fig. 2(a)]—and hence the progressive decrease of the band gap energy from the dome edge toward its center—leads excitons to drift toward the minimum energy available within their diffusion length before recombining [see Fig. 4(a)] [5,6].

Such a funnel effect, combined with the finite exciting/collecting area of the objective, alters the correspondence between the coordinate r (and thus ε_p) and the exciton energy derived from the emission spectra [6]. The solid curves displayed in Fig. 4(b) result from a fit performed by taking into account the exciton funneling (see Supplemental Material [28]), while fixing the radius of the collection area R_c to 2.5σ ($\sigma = 0.23\ \mu$m is the laser spot size [12]). The actual [i.e., free from the funnel effect; see Eq. (1)], "linearized" strain dependence of the A (I) exciton is shown in Fig. 4(b) as a blue (red) dashed line [44]. The surrounding shaded areas—covering the regions spanned by the trends computed for $2\sigma \leqslant R_c \leqslant 3\sigma$—represent the uncertainty of our

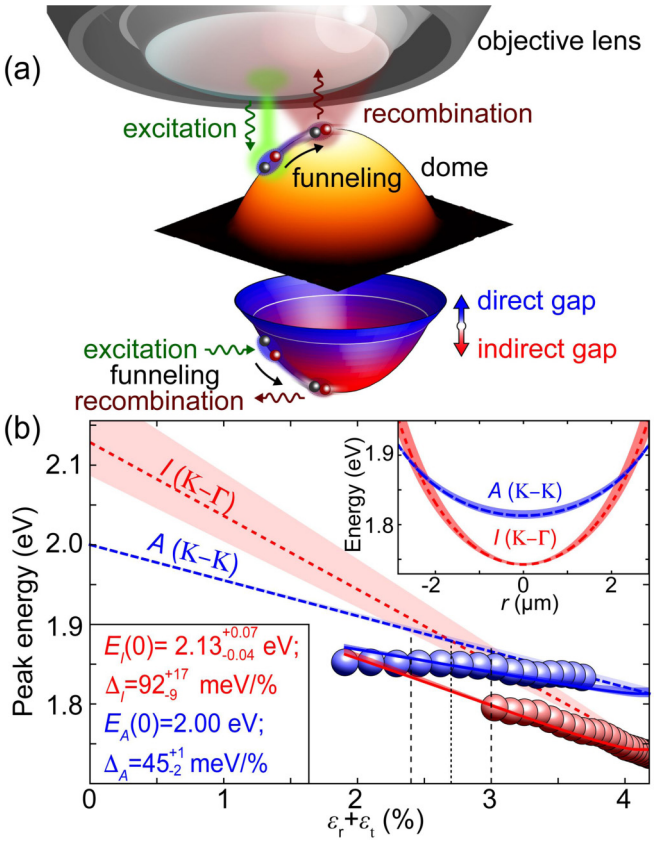

FIG. 4. (a) Sketch of a micro-PL experiment (excitation+recombination) on a single WS_2 dome (whose AFM image is shown in shaded orange), wherein an exciton drifts over the dome strain distribution (funnel effect [5,6]). The blue-red paraboloid provides a correspondence between the dome AFM image and the exciton energy, highlighting the direct-indirect transition region (see below). (b) Dependence of the energy of the direct (blue dots) and indirect (red dots) exciton transitions on the in-plane strain tensor, $\varepsilon_p = \varepsilon_r + \varepsilon_t$. The solid blue/red lines (relative to the direct/indirect exciton) are fits based on Eq. (1), while also taking funneling [see (a)] into account. These fits entail linear dependences of the exciton energies on ε_p, which are displayed as dashed lines; the shaded areas enveloping each curve account for the uncertainty of our fitting procedure (see main text). In turn, these linear dependences yield the evolution of the direct and indirect exciton energy across the dome, plotted in the inset of (b) [the paraboloid sketched in (a) is also based on this evolution].

procedure. This analysis permits to set the direct-to-indirect band gap crossover point at $\varepsilon_p = (2.7 \pm 0.3)\%$ highlighted by vertical dashed lines in Fig. 4(b). Finally, the top-right inset in Fig. 4(b) provides the A and I exciton energy as a function of the dome radial coordinate. The displayed fits yield $\Delta_A = 45^{+1}_{-2}$ meV/ε%, $E_I(0) = 2.13^{+0.07}_{-0.04}$ eV and $\Delta_I = 92^{+17}_{-9}$ meV/ε% [$E_A(0)$ is fixed to 2.00 eV, the strain-free ML exciton energy]. These data compare rather favorably with the experimental [35,45], and theoretical [17,18,20–22,24–27,46] ones as reported in Table I. However, we notice a large discrepancy between the $E_I(0)$-$E_A(0)$ value derived in this work (130 meV) and those reported in other works. In fact, these latter estimate the electronic band gap whereas our

TABLE I. Comparison between the data reported in this work and those in different experimental (Expt.) and theoretical (Theor.) works. $\Delta_{A(I)}$ indicates the shift rate with strain of the A (I) exciton energy. $E_I(0)$-$E_A(0)$ is the indirect-direct exciton energy difference at zero strain (though this quantity in the other works corresponds to the difference of the electronic band gap). $\varepsilon_{\text{transition}}$ is the equivalent uniaxial strain at which the band gap turns indirect.

		Our work	Expt. works	Theor. works
WS_2	Δ_A (meV/%)	45^{+1}_{-2}	46 [45], 47 [35]	59 [21], 67 [27], 66−75 [20]
	Δ_I/Δ_A	2.0		1.8−1.9 [20], 1.9 [27], 2.0 [21]
	$E_I(0)$-$E_A(0)$ (meV)	130^{+70}_{-40}	(280 ± 10) [26]	77 [21], 173 [46], 242 [20], 274 [27]
	$\varepsilon_{\text{transition}}$ (%)	2.7 ± 0.3		⩾2 [17,19,20,22,24,25,27]
MoS_2	Δ_A (meV/%)	37^{+3}_{-1}	(45 ± 3) [4], (45 ± 7) [32]	47 [21], 52−61 [20], 66 [27]
	Δ_I/Δ_A	2.5		2.0 [21], 2.1 [27], 2.3 [20]
	$E_I(0)$-$E_A(0)$ (meV)	100^{+80}_{-50}	∼300 [49]	13 [21], 110 [27], 127−184 [20], 148 [46]
	$\varepsilon_{\text{transition}}$ (%)	1.8 ± 0.7		⩾0.1 [5,17,19–21,23–25,27,32]

data embed exciton effects that are quite different for the A and I transitions: A heavier hole effective mass is reported in Ref. [26] at Γ ($m^h_\Gamma = 2.45m_0$, m_0 is the electron mass in vacuum) compared to K ($m^h_K = 0.48m_0$) that results in a difference between the indirect and direct exciton binding energy [47] equal to +144 meV [48]. In turn, this brings our 130 meV exciton value to a 274 meV electronic value, in close agreement with the other works' reported in Table I. We finally point out that we observed similar findings also in MoS_2 (see Table I) and WSe_2 [28].

In conclusion, we investigated the intertwined strain and electronic properties of spherically deformed TMD monolayers. We observed that sufficiently high tensile in-plane strains ($\varepsilon_p \sim 2.7\%$ in WS_2 ML, $\varepsilon_p \sim 1.5\%$ in MoS_2 ML, $\varepsilon_p \sim 2\%-3\%$ in WSe_2 ML [28]) turn a direct band gap material into an indirect-gap one. This general behavior must be considered when 2D crystals are to be employed in flexible optoelectronic devices, or possibly exploited for the observation of quantum many-body effects involving long-lived k-space indirect excitons [42].

We thank A. Surrente for comments and suggestions. We acknowledge support by Sapienza Università di Roma under the grants "Ricerche Ateneo" (A.P. and M.F.). M.F. and G.P. acknowledge support and funding from the Italian Ministry for Education, University and Research within the Futuro in Ricerca (FIRB) program (project DeLIGHTeD, Prot. RBFR12RS1W). This project has also received funding from the European Union's Horizon 2020 research and innovation Program No. 641899. We acknowledge fund support from Australian Research Council (ARC) (No. DE140100805 and No. DP180103238), and ARC Centre of Excellence in Future Low-Energy Electronics Technologies (Project No. CE170100039).

[1] Z. Dai, L. Liu, and Z. Zhang, Strain engineering of 2D materials: Issues and opportunities at the interface, Adv. Mater. **31**, 1805417 (2019).

[2] B. Amorim, A. Cortijo, F. de Juan, A. G. Grushin, F. Guinea, A. Gutiérrez-Rubio, H. Ochoa, V. Parente, R. Roldán, P. San-Jose, J. Schiefele, M. Sturla, and M. A. H. Vozmediano, Novel effects of strains in graphene and other two dimensional materials, Phys. Rep. **617**, 1 (2016).

[3] S. Deng, A. V. Sumant, and V. Berry, Nano Today **22**, 14 (2018).

[4] D. Lloyd, X. Liu, J. W. Christopher, L. Cantley, A. Wadehra, B. L. Kim, B. B. Goldberg, A. K. Swan, and J. S. Bunch, Band gap engineering with ultralarge biaxial strains in suspended monolayer MoS_2, Nano Lett. **16**, 5836 (2016).

[5] J. Feng, X. Qian, C.-W. Huang, and J. Li, Strain-engineered artificial atom as a broad-spectrum solar energy funnel, Nat. Photonics **6**, 866 (2012).

[6] A. Castellanos-Gomez, R. Roldan, E. Cappelluti, M. Buscema, F. Guinea, H. S. J. van der Zant, and G. A. Steele, Local strain engineering in atomically thin MoS_2, Nano Lett. **13**, 5361 (2013).

[7] H. Ochoa, R. Zarzuela, and Y. Tserkovnyak, Emergent gauge fields from curvature in single layers of transition-metal dichalcogenides, Phys. Rev. Lett. **118**, 026801 (2017).

[8] D. Tedeschi, E. Blundo, M. Felici, G. Pettinari, B. Liu, T. Yildrim, E. Petroni, C. Zhang, Y. Zhu, S. Sennato, Y. Lu, and A. Polimeni, Controlled micro/nanodome formation in proton-irradiated bulk transition-metal dichalcogenides, Adv. Mater. **31**, 1903795 (2019).

[9] R. Trotta, A. Polimeni, F. Martelli, G. Pettinari, M. Capizzi, L. Felisari, S. Rubini, M. Francardi, A. Gerardino, P. C. M. Christianen, and J. C. Maan, Fabrication of site-controlled quantum dots by spatially selective incorporation of hydrogen in Ga(AsN)/GaAs heterostructures, Adv. Mater. **23**, 2706 (2011).

[10] M. Seel and R. Pandey, Proton and hydrogen transport through two-dimensional monolayers, 2D Mater. **3**, 025004 (2016).

[11] E. Khestanova, F. Guinea, L. Fumagalli, A. Geim, and I. Grigorieva, Universal shape and pressure inside bubbles appearing in van der Waals heterostructures, Nat. Commun. **7**, 12587. (2016).

[12] The laser spot size resulting from the NA = 0.9 objective employed for micro-Raman and micro-PL mapping was experimentally determined as follows: The laser was scanned across a reference sample, lithographically patterned with features of known width (1 μm). The intensity of the reflected light was fitted with the ideal reflectance profile, convolved with a Gaussian

peak. The standard deviation of this peak, obtained as a fitting parameter, provides our estimate of $\sigma = 0.23 \pm 0.01\ \mu$m.

[13] Z. Jia, J. Dong, L. Liu, A. Nie, J. Xiang, B. Wang, F. Wen, C. Mu, Z. Zhao, B. Xu, Y. Gong, Y. Tian, and Z. Liu, Photoluminescence and Raman spectra oscillations induced by laser interference in annealing-created monolayer WS_2 bubbles, Adv. Opt. Mater. **7**, 1801373 (2019).

[14] K. Yue, W. Gao, R. Huang, and K. M. Liechti, Analytical methods for the mechanics of graphene bubbles, J. Appl. Phys. **112**, 083512 (2012).

[15] P. Wang, W. Gao, Z. Cao, K. M. Liechti, and R. Huang, Numerical analysis of circular graphene bubbles, J. Appl. Mech. **80**, 040905 (2013).

[16] W. B. Fichter, Some solutions for the large detections of uniformly loaded circular membranes, NASA Technical Report No. NASA-TP-3658, 1997 (unpublished).

[17] P. Johari and V. B. Shenoy, Tuning the electronic properties of semiconducting transition metal dichalcogenides by applying mechanical strains, ACS Nano **6**, 5449 (2012).

[18] S. Horzum, H. Sahin, S. Cahangirov, P. Cudazzo, A. Rubio, T. Serin, and F. M. Peeters, Phonon softening and direct to indirect band gap crossover in strained single-layer $MoSe_2$, Phys. Rev. B **87**, 125415 (2013).

[19] M. Ghorbani-Asl, S. Borini, A. Kuc, and T. Heine, Strain-dependent modulation on conductivity in single-layer transition-metal dichalcogenides, Phys. Rev. B **87**, 235434 (2013).

[20] H. Shi, H. Pan, Y.-W. Zhang, and B. I. Yakobson, Quasiparticle band structures and optical properties of strained monolayer MoS_2 and WS_2, Phys. Rev. B **87**, 155304 (2013).

[21] C.-H. Chang, X. Fan, S.-H. Lin, and J.-L. Kuo, Orbital analysis of electronic structure and phonon dispersion in MoS_2, $MoSe_2$, WS_2, and WSe_2 monolayers under strain, Phys. Rev. B **88**, 195420 (2013).

[22] B. Amin, T. P. Kaloni, and U. Schwingenschl, Strain engineering of WS_2, WSe_2, and WTe_2, RCS Adv. **4**, 34561 (2014).

[23] R. Das, B. Rakshit, S. Debnath, and P. Mahadevan, Microscopic model for the strain-driven direct to indirect band-gap transition in monolayer MoS_2 and ZnO, Phys. Rev. B **89**, 115201 (2014).

[24] L. Ortenzi, L. Pietronero, and E. Cappelluti, Zero-point motion and direct-indirect band-gap crossover in layered transition-metal dichalcogenides, Phys. Rev. B **98**, 195313 (2018).

[25] L. Wang, A. Kutana, and B. I. Yakobson, Many-body and spin-orbit effects on direct-indirect band gap transition of strained monolayer MoS_2 and WS_2, Ann. Phys. **526**, L7 (2014).

[26] L. Waldecker, A. Raja, M. Rösner, C. Steinke, A. Bstwick, R. J. Koch, C. Jozwiak, T. Taniguchi, K. Watanabe, E. Rotenberg, T. O. Wehling, and T. F. Heinz, Rigid Band Shifts in Two-Dimensional Semiconductors through External Dielectric Screening, Phys. Rev. Lett. **123**, 206403 (2019).

[27] K. Zollner, P. E. Faria Junior, and J. Fabian, Strain-tunable orbital, spin-orbit, and optical properties of monolayer transition-metal dichalcogenides, Phys. Rev. B **100**, 195126 (2019).

[28] See Supplemental Material at http://link.aps.org/supplemental/10.1103/PhysRevResearch.2.012024 for a detailed description of micro-Raman experiments, effect of dome capping on the dome volume versus T, funneling effect details, and results found in other 2D TMDs.

[29] F. Wang, I. A. Kinloch, D. Wolverson, R. Tenne, A. Zak, E. O'Connell, U. Bangert, and R. J. Young, Strain-induced phonon shifts in tungsten disulphide nanoplatelets and nanotubes, 2D Mater. **4**, 015007 (2017).

[30] A. M. Dadgar, D. Scullion, K. Kang, D. Esposito, E.-H. Yang, I. P. Herman, M. A. Pimenta, E.-J. G. Santos, and A. N. Pasupathy, Achieving large, tunable strain in monolayer transition-metal dichalcogenides, Chem. Mater. **30**, 5148 (2018).

[31] S. B. Desai, G. Seol, J. S. Kang, H. Fang, C. Battaglia, R. Kapadia, J. W. Ager, J. Guo, and A. Javey, Strain-induced indirect to direct bandgap transition in multilayer WSe_2, Nano Lett. **14**, 4592 (2014).

[32] H. J. Conley, B. Wang, J. I. Ziegler, R. F. Haglund, Jr., S. T. Pantelides, and K. I. Bolotin, Bandgap engineering of strained monolayer and bilayer MoS_2, Nano Lett. **13**, 3626 (2013).

[33] Q. Zhang, Z. Chang, G. Xu, Z. Wang, Y. Zhang, Z.-Q. Xu, S. Chen, Q. Bao, J. Z. Liu, Y.-W. Mai, W. Duan, M. S. Fuhrer, and C. Zheng, Strain relaxation of monolayer WS_2 on plastic substrate, Adv. Funct. Mater. **26**, 8707 (2016).

[34] R. Yang, J. Lee, S. Ghosh, H. Tang, R. M. Sankaran, C. A. Zorman, and P. X.-L. Feng, Tuning optical signatures of single- and few-layer MoS_2 by blown-bubble bulge straining up to fracture, Nano Lett. **17**, 4568 (2017).

[35] R. Frisenda, M. Drüppel, R. Schmidt, S. M. de Vasconcellos, D. P. de Lara, R. Bratschitsch, M. Rohlfing, and A. Castellanos-Gomez, Biaxial strain tuning of the optical properties of single-layer transition metal dichalcogenides, 2D Mater. **1**, 10 (2017).

[36] J. Chaste, A. Missaoui, S. Huang, H. Henck, Z. Ben Aziza, L. Ferlazzo, C. Naylor, A. Balan, A. T. C. Johnson, Jr., R. Braive, and A. Ouerghi, Intrinsic Properties of suspended MoS_2 on SiO_2/Si pillar arrays for nanomechanics and optics, ACS Nano **12**, 3235 (2018).

[37] Y. Wang, C. Cong, W. Yang, J. Shang, N. Peimyoo, Y. Chen, J. Kang, J. Wang, W. Huang, and T. Yu, Strain-induced direct-indirect bandgap transition and phonon modulation in monolayer WS_2, Nano Res. **8**, 2562 (2015).

[38] J. Pető, G. Dobrik, G. Kukucska, P. Vancsó, A. A. Koós, J. Koltai, P. Nemes-Incze, C. Hwang, and L. Tapasztó, Moderate strain induced indirect bandgap and conduction electrons in MoS_2 single layers, 2D Mater Appl. **3**, 39 (2019).

[39] C. Ma, J. Yan, Y. Huang, Z. Zheng, and G. Yang, Direct-indirect bandgap transition in monolayer MoS_2 induced by an individual Si nanoparticle, Nanotechnology **31**, 065204 (2019).

[40] C. Robert, D. Lagarde, F. Cadiz, G. Wang, B. Lassagne, T. Amand, A. Balocchi, P. Renucci, S. Tongay, B. Urbaszek, and X. Marie, Exciton radiative lifetime in transition metal dichalcogenide monolayers, Phys. Rev. B **93**, 205423 (2016).

[41] H. Liu, T. Wang, C. Wang, D. Liu, and J. Luo, Exciton radiative recombination dynamics and nonradiative energy transfer in two-dimensional transition-metal dichalcogenides, J. Phys. Chem. C **123**, 10087 (2019).

[42] J. J. Esteve-Paredes, S. Pakdel, and J. J. Palacios, Quenching of Exciton Recombination Unstrained Two-Dimensional Monochalcogenides, Phys. Rev. Lett. **123**, 077402 (2019).

[43] Y. Sun, S. E. Thompson, and T. Nishida, *Strain Effect in Semiconductors: Theory and Device Applications* (Springer, New York, 2010), Chap. 2.

[44] We note that the agreement between the model and the experimental data is less good for the *A* exciton with respect to the *I* exciton. This is caused by the presence of small domes close to the edges of the largest domes (namely, where the *A* exciton

dominates) that adds to the effect of the finite resolution of our optical system and of funneling phenomena.

[45] X. He, H. Li, Z. Zhu, Z. Dai, Y. Yang, P. Yang, Q. Zhang, P. Li, U. Schwingenschlogl, and X. Zhang, Strain engineering in monolayer WS_2, MoS_2, and the WS_2/MoS_2 heterostructure, Appl. Phys. Lett. **109**, 173105 (2016).

[46] Z. Jin, X. Li, J. T. Mullen, and K. W. Kim, Intrinsic transport properties of electrons and holes in monolayer transition-metal dichalcogenides, Phys. Rev. B **90**, 045422 (2014).

[47] A. Chernikov, T. C. Berkelbach, H. M. Hill, A. Rigosi, Y. Li, O. B. Aslan, D. R. Reichman, M. S. Hybertsen, and T. F. Heinz, Exciton Binding Energy and Nonhydrogenic Rydberg Series in Monolayer WS_2, Phys. Rev. Lett. **113**, 076802 (2014).

[48] The 144-meV difference was evaluated by using $m_K^e = 0.63 m_K^h$ derived from Ref. [26] and considering a binding energy for the *A* exciton equal to 320 meV [47].

[49] H. Yuan, Z. Liu, G. Xu, B. Zhou, S. Wu, D. Dumcenco, K. Yan, Y. Zhang, S.-K. Mo, P. Dudin, V. Kandyba, M. Yablonskikh, A. Barinov, Z. Shen, S. Zhang, Y. Huang, X. Xu, Z. Hussain, H. Y. Hwang, Y. Cui, and Y. Chen, Evolution of the valley position in bulk transition-metal chalcogenides and their monolayer limit, Nano Lett. **16**, 4738 (2016).